







**Optimization of Bragg scattering from atomic gratings for echo interferometry**Gehrig Carlse <sup>\*</sup>, Jaskaran Randhawa , Eduardo Ramos , Thomas Vacheresse, Alex Pouliot , Adam C. Carew , and A. Kumarakrishnan <sup>†</sup><sup>1</sup>*Department of Physics and Astronomy, York University, Toronto, Ontario, Canada M3J 1P3*Brynle Barrett *Department of Physics, 8 Bailey Drive, University of New Brunswick, Fredericton, New Brunswick, Canada E3B 5A3*

(Received 25 July 2024; accepted 19 September 2024; published 8 October 2024)

We investigate the characteristics of near resonant Bragg scattering, the underlying process that produces a signal in a grating-echo atom interferometer. We explore how the density modulation produced in an atomic sample by momentum state interference and optical channeling can be optimally read out using a coherently Bragg-scattered traveling-wave electric field. When both the channeling and Bragg scattering processes are optimized, we report a 20-fold increase in scattering efficiency. Our results suggest that a quantitative understanding of the atomic confinement achievable by channeling is possible through an analysis of reflectivity spectra.

DOI: [10.1103/PhysRevA.110.043306](https://doi.org/10.1103/PhysRevA.110.043306)**I. INTRODUCTION**

In the 35 years since its initial realization, the Raman atom interferometer (AI) [1–4], has become an indispensable tool for precision measurements of inertial effects [5–8] and fundamental physical constants [9–18]. Due to widespread adaptation for remote sensing [19–24], the strengths and limitations of the Raman AI have been thoroughly analyzed [25–27]. Another class of interferometers that has been explored for precision measurements is the Bragg AI [28–35]. However, assessments of other interferometers that may be able to realize comparable performance have lagged behind. One such potentially simpler and underutilized technique is the grating-echo AI [36–38] which has achieved measurements of  $\hbar/m$  and gravitational acceleration ( $g$ ) with a lower sensitivity of about 50 parts per  $10^9$  (ppb) [39,40]. However, improvements in the performance of grating-echo AIs can be achieved by channeling atoms [41,42]. In this paper, we show that further improvements are possible by optimizing the Bragg scattering process that is central to the detection of matter-wave interference in echo AIs.

The grating-echo AI [36], which can be regarded as a form of the Talbot-Lau interferometer [43–46], is a single state AI which uses Kapitza-Dirac diffraction [47,48] of atomic momentum states to generate matter-wave interference. The enclosed area of representative space-time paths of atomic waves for a grating-echo AI is shown in Fig. 1. The AI involves excitation of a laser-cooled atomic sample by two temporally separated optical standing wave (SW) pulses with a delay time  $T$ . The interference of momentum states can be visualized using the “billiard ball” model [49].

After the first SW pulse, Kapitza-Dirac diffraction of momentum states leads to matter-wave interference and the formation of a density grating with a spatial period of  $\lambda/2$ , where  $\lambda$  is the wavelength of the SW excitation. This density modulation is transient due to Doppler dephasing of the momentum states and it can be probed with a traveling-wave readout pulse applied immediately after the SW excitation (at time  $t = 0$ ). This configuration is called the one-pulse grating AI. If the atoms remain within the interaction zone established by the laser excitation, it is possible to apply a second SW pulse (at  $t = T$ ) to cancel the Doppler phases of the momentum states at an echo time ( $t = 2T$ ). This causes the density modulation to rephase in the vicinity of the echo time even a long time after it has otherwise washed out. The rephased density grating can also be probed with a traveling-wave readout pulse. The dual SW pulse configuration is called the grating-echo AI, drawing its name from the well-known photon echo effect [50]. Both the one-pulse grating AI and the grating-echo AI are represented in Fig. 1.

Precision measurements using the echo AI require the density modulation to be probed across a range of pulse separations  $T$ . A determination of  $\hbar/m$  relies on measuring the recoil modulation present in the backscattered field amplitude. A measurement of  $g$  relies on recording the phase accumulation in the backscattered light due to the falling grating. The sensitivity in both of these measurements stems from the ability to resolve the echo signal for large excitation pulse separations. In order to exploit these long timescales, it is critically important to maximize the signal-to-noise ratio of the readout process. In this paper, we study the spectral features of near-resonant Bragg scattering as a means to augment the backscattered signal.

We note that optimization strategies have been achieved in other AI schemes. For instance, in Raman AIs, losses in overall atom number (imposed by velocity selection and magnetic state preparation) have been overcome by utilizing

<sup>\*</sup>Contact author: [gehrig.carlse@gmail.com](mailto:gehrig.carlse@gmail.com)<sup>†</sup>Contact author: [akumar@yorku.ca](mailto:akumar@yorku.ca)

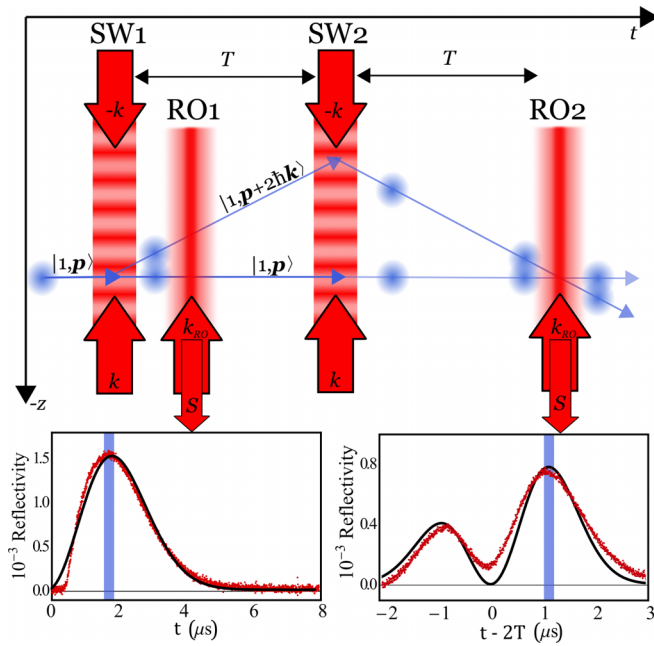


FIG. 1. Schematic of one-pulse grating AI and grating-echo AI using the “billiard ball” model, where the excitation (SW,  $\pm k = 2\pi/\lambda$ ) and readout (RO,  $k_{\text{RO}}$ ) are incident along the  $z$  direction. For simplicity, only one set of interfering trajectories is shown for a generic ground state  $|1, p\rangle$ . The backscattered signal is indicated by  $S$ . The lower panels show experimental data (points) for the one-pulse grating AI (left) and the grating-echo AI (right) for a sample of  $^{85}\text{Rb}$  with a temperature of  $\approx 10\ \mu\text{K}$ . The vertical bars indicate the reflectivity integration window described in Sec. II. Data are overlaid with an analytic model of the echo envelope in the Raman-Nath regime (solid black lines) described in Appendix B.

population measurements at the output ports that involve scattering several thousand photons per atom. Similarly, contrast interferometers, such as Talbot-Lau AIs using Bose-Einstein condensates (BECs), have been able to leverage the narrowness of the condensate velocity distribution to record several periods of the recoil modulation using a single readout pulse, resulting in improved sensitivity [51,52].

Although a number of grating-echo AI techniques using cold atoms have been developed to measure recoil [39,53–56],  $g$  [40,57], magnetic field gradients [57,58], and the velocity distribution of atomic samples [37], these measurements have not optimized the backscattered signal. In general, these measurements have operated with far off-resonant probe/readout detunings ( $\Delta_{\text{RO}} > 50\ \text{MHz}$ ) to reduce the effects of spontaneous emission and with short excitation pulses in an effort to satisfy the Raman-Nath criterion where theory is available to describe the momentum state interference [37,38,54,59]. As a consequence, the grating reflectivity in these studies has been restricted to  $\approx 0.1\%$  due to the low contrast of density modulation produced by SW excitation. Correspondingly, the timescale of past experiments has been restricted to  $T \approx 50\ \text{ms}$ .

Despite these limitations, by virtue of operating with a single ground state, an excitation scheme that uses only a single laser without the technical complexities of phase locked lasers to drive the Raman transitions, losses associated with velocity

selection, or the requirements of BEC sample preparation, the grating-echo AI offers a relatively simple alternative to the Raman AI and BEC Talbot-Lau AIs.

A particularly attractive feature of the echo AI is that the backscattered signal in response to the readout pulse arises due to coherent Bragg scattering from a phased array of dipoles. The amplitude of this signal can be increased by improving the contrast of the density modulation. In addition, this signal exhibits a nonlinear scaling as a function of the number of participating atoms and the relative detuning of the readout pulse. While these features of coherent scattering have been demonstrated in other optical crystals [60,61], they have not been fully exploited in the context of the echo AI.

Recently, there have been renewed efforts to improve the contrast of the echo AI by channeling atoms into a SW lattice [41,42,62] and to understand the underlying coherent scattering processes that give rise to the signal. In the context of our experiments, channeling refers to the application of long excitation pulses that violate the Raman-Nath criterion. In a classical description, this type of excitation results in the relocation of atoms to the nodes of the SW potential. Channeling in this manner increases the overall contrast of the density modulation arising from matter-wave interference and leads to more efficient Bragg scattering. In particular, Ref. [42] has shown the effectiveness of channeling performed during trap loading, while our previous work [41] demonstrated a similar sixfold increase in reflectivity while performing channeling after the trapping forces have been turned off.

In this paper, we build on the developments of Ref. [41] and investigate how the Bragg reflectivity of a channeled grating-echo AI can be maximized. We explore the dependence of Bragg scattering on the detuning of the readout field, the number of atoms in the cold sample, and the degree of localization of the atoms that is controlled by the channeling effects of the excitation pulses. We support this paper with numerical simulations of optical channeling and Bragg scattering using a transfer matrix formalism [61,63]. We interpret our measurements on the basis of these simulations, which predict the expected enhancement in the AI reflectivity over a broad range of channeling times and readout detunings. We demonstrate that a 20-fold improvement in reflectivity can be achieved for the one-pulse grating AI by optimizing the channeling and Bragg scattering processes. We show that a similar improvement can be replicated in the grating-echo AI. The enhanced peak reflectivity in echo experiments demonstrated in this paper renews the possibility of extending the timescale of echo AI measurements to improve sensitivity.

We have organized the remainder of the paper as follows: the experimental setup is described in Sec. II, the theoretical model used to characterize Bragg scattering in the echo AI is explained in Sec. III, and the results and discussion are presented in Sec. IV.

## II. EXPERIMENTAL SETUP

The experimental setup and trapping scheme are the same as described in Ref. [41]. A cloud of  $\approx 10^9$   $^{85}\text{Rb}$  atoms with a density of  $\approx 10^{10}\ \text{cm}^{-3}$  and a temperature of  $\approx 10\ \mu\text{K}$  is released from a vapor cell loaded magneto-optical trap (MOT)

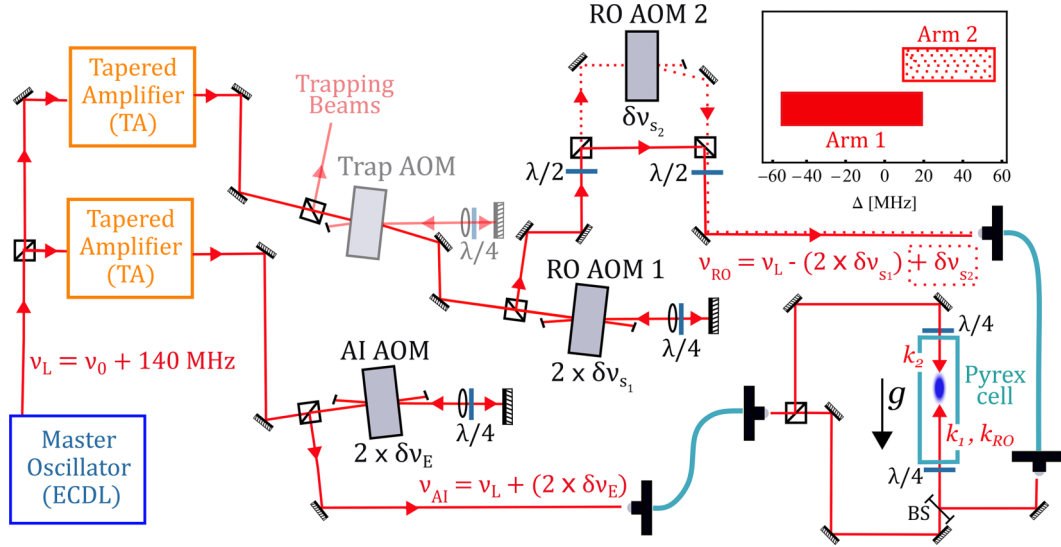


FIG. 2. Schematic of the frequency shifts for AI and RO pulses. The AI beams are generated from a dual-pass AOM (AI AOM,  $\delta v_E = 125$  MHz) resulting in a detuning of  $\Delta_{AI} \approx 390$  MHz. The RO is derived from the undiffracted beam of the trapping AOM. The RO is downshifted by a separate dual-pass AOM (RO AOM 1), shown by the solid beam path, labeled Arm 1. The resulting frequency shift is  $2\delta v_{s1}$  where  $\delta v_{s1} \in [-60, -95]$  MHz. For additional tuning range, the output of RO AOM 1 can also be directed into a single pass AOM (RO AOM 2), that results in an additional frequency shift of  $\delta v_{s2} \in [70, 90]$  MHz. This beam path, labeled Arm 2, is indicated by the dashed line. The full tuning range using both RO arms is shown as an inset. All detunings are with respect to the  $F = 3 \rightarrow F' = 4'$  transition in  $^{85}\text{Rb}$  ( $\nu_0$ ). The directions of the beams relative to the trapping cell and  $g$  are also shown. Legend:  $\lambda/4$ , quarter waveplate;  $\lambda/2$ , half waveplate; BS, 50:50 nonpolarizing beamsplitter.

[64] at the center of a  $\approx 1$ -m Pyrex tube with rectangular faces. Typically, the MOT has an ellipsoidal shape, with a horizontal extent of  $\approx 6$  mm and a vertical length of  $\approx 12$  mm. The trapping, repumping, AI excitation, and readout beams are derived from master-oscillator power amplifier (MOPA) systems seeded by external cavity diode lasers that have nominal linewidths of  $\approx 200$  kHz [65,66]. These beams are routed to the Pyrex cell using optical fibers, as shown in Fig. 2.

The size of the MOT is imaged on a CCD camera and the number of atoms,  $N$ , is inferred from fluorescence [59,67,68].  $N$  is varied by changing the repetition rate of the experiment, the intensity of the repump light, and the magnetic field gradient of the trapping coils.

The AI excitation is composed of two circularly polarized pulses ( $\sigma^+ - \sigma^+$ ) counterpropagating along the vertical direction. To reduce the effect of spontaneous emission during the excitation, these pulses are tuned  $\approx 390$  MHz above  $\nu_0$ , the  $F = 3 \rightarrow F' = 4'$  transition in  $^{85}\text{Rb}$ . This is accomplished using a 125-MHz acousto-optic modulator (AOM) operated in dual-pass configuration [69,70] which also reduces optical leakage into the AI. As in Ref. [41], these channeling excitation pulses are applied after the MOT has been released from an optical molasses.

In order to study near-resonant Bragg scattering of a probe beam, we tune the readout pulse over a range of  $\nu_0 \pm 50$  MHz using separate chains of AOMs (Arm 1 and Arm 2 in Fig. 2). To facilitate this tuning range, after the MOT is released, we generate the traveling-wave readout pulse from the same MOPA system which drives the trapping beams. We show the relevant beam paths and frequency shifts in Fig. 2. The AI excitation beams are spatially overlapped with the readout beam using a 50:50 beamsplitter. All of these pulses have

nominal beam waists of  $\approx 3$  mm. In these experiments, the readout power varies in the range of 1–10 mW, while the excitation pulses generally have powers of  $\approx 10$  mW. This excitation intensity corresponds to a single beam Rabi frequency of  $\Omega_1 = \Gamma \sqrt{I/2I_s} \approx 3\Gamma$ , where  $\Gamma$  is the radiative rate of the excited state,  $I$  is the single beam intensity, and  $I_s = 3.9 \text{ mW/cm}^2$  is the saturation intensity. The Rabi frequency of the standing wave is then defined as  $\Omega_0 = \Gamma \sqrt{I/I_s} \approx 4.2\Gamma$ .

As in Ref. [41], the backscattered signals from the AI are collected using a photomultiplier tube gated both by an electronic circuit (rise time  $\approx 200$  ns) and by a 250-MHz AOM ( $\approx 20\%$  efficiency and  $\approx 100$ -ns rise time). Traces are collected with a digital oscilloscope with a bandwidth of 80 MHz. We measure the power of the readout beam using a calibrated photodiode and calculate the reflected fraction of the readout light from the atomic sample. Here we assume that the scattered beam has the same spatial extent as the readout beam and compute reflectivity as the ratio of the power in the incoming and reflected beams. We measure this reflectivity across a small time window of the scattered field envelope where the signal is maximized, as shown in Fig. 1, and report the average of four to eight repetitions. Error bars in the figures that follow represent the standard deviation of these repeated measurements.

### III. THEORETICAL CONSIDERATIONS

In a simplistic picture, when a density modulation is established in an atomic ground state, a traveling-wave readout pulse can be used to create superpositions between ground and excited states so that emission from an array of dipole oscillators emerges as a coherent burst along a phase matched

direction. Such a description of Bragg scattering can be used to understand the signal in both the one-pulse grating AI and the grating-echo AI. However, to include the effects of sample density and pulse propagation, it is necessary to describe Bragg scattering in a more rigorous manner.

In an effort to quantitatively model the reflectivity of the grating-echo AI, we begin with the reflection coefficient for a lattice formed in a dilute gas. As shown in Appendix A, we follow Refs. [50,61,63,71] and assume that the reflection coefficient is given by

$$R = \frac{18}{\pi^4} \left( \frac{\lambda_{\text{RO}}}{D} \right)^4 \frac{S_{F,F'}^2}{1 + (2\Delta_{\text{RO}}/\Gamma)^2} (f_R N)^2 \beta^2 \quad (1)$$

where  $D$  is the diameter of the backscattered beam,  $\lambda_{\text{RO}}$  is the scattering field (readout) wavelength,  $\Delta_{\text{RO}}$  is the detuning of the readout beam from the excited state resonance, and  $S_{F,F'}$  is the oscillator strength of the resonant hyperfine transition  $F$  to  $F'$ .  $N$  is the number of atoms in the sample and  $f_R$  represents the fraction of atoms participating in the scattering which is akin to the occupation number of the lattice [72], while  $\beta = e^{-2\sigma_z^2 k_{\text{RO}}^2}$  is the Debye-Waller factor, characterizing the relative localization  $\sigma_z$  of the atoms in the lattice.

While Eq. (1) captures the key features of the backscattered signal, it is valid only in the limit of far off-resonant readout light (“conventional” Bragg scattering) or in the near-resonant case for very dilute vapors, where absorption is minimal and multiple scattering events are negligible. Under these conditions, the characteristics of the optical lattice in the dilute gas can be quantified using the Debye-Waller factor [73], which describes the degree of confinement of atoms. Equation (1) clearly shows the linkage between higher reflectivity and the increase in grating contrast parametrized by  $\beta^2$ .

On the basis of this treatment, we can also predict increased reflectivity with (i) samples containing more atoms and (ii) near-resonance readout excitation. However, increasing the number of atoms in the sample to leverage the  $N^2$  dependence and decreasing the readout detuning to exploit the Lorentzian spectral shape begin to violate the assumptions underlying Eq. (1). Accordingly, a more nuanced approach is necessary to describe the improvements that can be achieved in our experiments by changing these parameters to maximize Bragg scattering in the grating-echo AI.

While the basis of the backscattered signal from the echo AI is a result of momentum state interference, Ref. [41] has shown that the variation in atomic density along the lattice direction is enhanced by optical channeling when pulses violate the Raman-Nath criterion. In this configuration, the transfer matrix (or  $ABCD$  matrix) is particularly well suited to describe the propagation, reflection, and absorption of light through a medium of varying density [61,72,74,75]. Accordingly, we use a simplified transfer matrix formalism to express the scattering from the atomic sample. We combine this with a model of atomic channeling similar to Ref. [41] to describe the experimental data more fully, as described below.

### A. Transfer matrices and sequential density model

We consider a sample of volume  $V$  with a length  $L$  in the  $z$  direction, as shown in Fig. 3(a). To employ the transfer matrix approach, we partition the full sample into thin slices

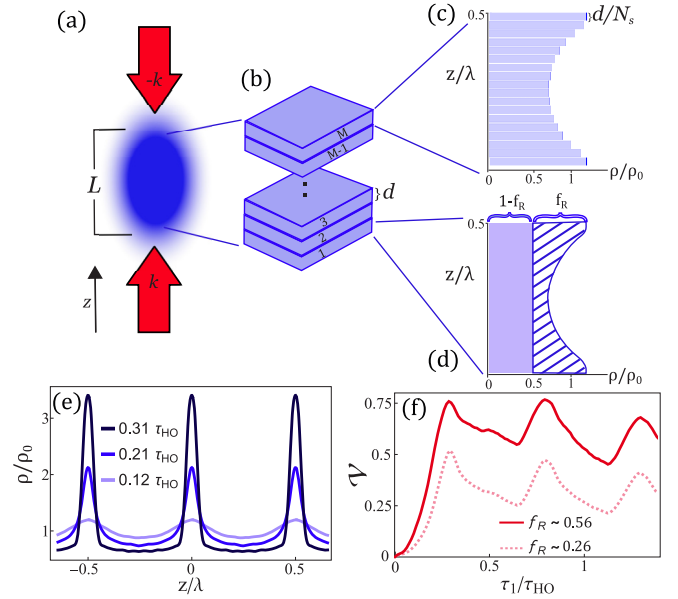


FIG. 3. (a) Excitation geometry of the atomic sample. (b) Approximation of the atomic volume with a flat-top profile made up of  $M = L/d$  scattering units, where  $d = \lambda/2$  is the lattice period. (c) Partitioning of scattering unit into  $N_s$  sublayers each of length  $\delta z = \lambda/40$ , where the atomic population distribution  $\rho$  is shown relative to the unmodulated density  $\rho_0$ . (d) Differentiates between the effective interacting fraction  $f_R$  (hashed area) and the remaining atomic density (solid area). (e) The effect of channeling in the SW potential. (f) Calculations of  $\rho(z)/\rho_0$  across one optical lattice wavelength for various channeling times, using Eqs. (8) and (9) for 1000 atoms with  $f_R = 0.5$ . (f) Lattice visibility [from Eq. (11)] as a function of channeling time for different values of  $f_R$ , corresponding to the one-pulse grating and grating-echo AI.

of approximately uniform density that occupy the  $xy$  plane. To characterize light propagation through each small transverse slice, we write the reflectivity of a thin layer located at a position  $z$  as

$$\zeta(z) = -\rho(z) \frac{3\delta z}{(k_{\text{RO}} \cos \gamma)^2} A_{F,F'} \quad (2)$$

where  $\rho(z)$  is the density of the thin layer with thickness  $\delta z$ ,  $k_{\text{RO}}$  is the wave vector of the readout beam, and  $\gamma$  is the angle between  $k_{\text{RO}}$  and the  $z$  direction.

To incorporate contributions from all nearby excited states we include the overall transition strength:

$$A_{F,F'} = \sum_{F,F'} \frac{S_{F,F'}}{(i + 2\Delta_{F,F'}/\Gamma)} \quad (3)$$

where  $\Delta_{F,F'}$  is the detuning of the readout beam from each resonant transition parametrized by the oscillator strength  $S_{F,F'}$ .

We then follow Refs. [61,71,72] and write a transfer matrix for an individual layer:

$$\mathcal{M}_{\delta z} = \begin{pmatrix} 1 + i\zeta e^{ik_{\text{RO}}\delta z \cos \gamma} & i\zeta e^{-ik_{\text{RO}}\delta z \cos \gamma} \\ -i\zeta e^{ik_{\text{RO}}\delta z \cos \gamma} & 1 - i\zeta e^{-ik_{\text{RO}}\delta z \cos \gamma} \end{pmatrix}. \quad (4)$$



The transfer matrix for the entire sample then becomes

$$\mathcal{M} = \prod_{j=1}^K \mathcal{M}_{\delta z}(j\delta z) \quad (5)$$

where  $K = L/\delta z$  is the integer number of thin sequential layers and the reflection coefficient for the sample can be expressed as

$$R = \left| \frac{\mathcal{M}_{1,2}}{\mathcal{M}_{2,2}} \right|^2 \quad (6)$$

where  $\mathcal{M}_{1,2}$  and  $\mathcal{M}_{2,2}$  represent the (1,2) and (2,2) indexed elements of the transfer matrix. Additionally, the transmissivity of the sample is given by  $T = |1/\mathcal{M}_{2,2}|^2$ , and the absorbed fraction of readout light is  $A = 1 - T - R$ . This last quantity is a measure of incoherently scattered photons due to spontaneous emission.

The sequential density model [Eqs. (2)–(6)] describes the evolution of the optical field amplitude and phase as the light propagates through discrete layers of an arbitrary one-dimensional atomic density distribution. This model is valid across both the thin- and thick-grating regimes [61]. The latter is characterized by multiple reflections between atomic layers, and can lead to the suppression of spontaneous emission due to photonic band gaps in the atomic lattice [72]. Our experiments operate in an intermediate regime, between the thin- and thick-grating limits, with a significant portion of the density distribution corresponding to disordered atoms.

Similar to Eq. (1), which is valid in the thin-grating limit, the sequential density model predicts an enhanced reflectivity as the readout frequency is tuned toward an atomic transition. This arises due to periodic structures in the atomic density that meet the condition for coherent Bragg scattering and increased atom-field coupling with the excited state. However, as the readout field approaches resonance, the contribution from incoherent scattering due to absorption/spontaneous emission also increases. Consequently, both  $R$  and  $T$  decrease near  $\Delta_{\text{RO}} = 0$ . These competing processes are captured in the overall transition strength [Eq. (3)] which is embedded in the sequential density model [Eqs. (2)–(6)]. For our experimental conditions, this behavior tends to produce a reflectivity spectrum with a dip around the  $F = 3 \rightarrow 4$  resonance of  $^{85}\text{Rb}$ . We discuss the shape of the spectra further in Sec. IV.

For this paper, we determine the length of the sample  $L$  using a CCD image of the cloud and assume a top-hat profile with an extent equal to the  $1/e$  full width of the image. As shown in Fig. 3(b), we deconstruct the atomic sample into  $M = L/d$  scattering units along the lattice direction each with thickness  $d = \lambda/2$  representing a single period of the lattice. In order to capture density variation across the lattice period, like that arising from optical channeling, each scattering unit is then further partitioned into  $N_s = 20$  sublayers each with a thickness  $\delta z = \lambda/40$ , as illustrated in Fig. 3(c). This leads to a full transfer matrix of  $K = M \times N_s$  layers. Since in our experiments  $L$  is on the order of  $\approx 1$  cm, typically we have  $M \approx 3 \times 10^4$  lattice periods and  $K \approx 6 \times 10^5$  sublayers in the sample. It is in the calculation of these sublayer densities that the effects of channeling are incorporated.

## B. Channeled distributions

We consider the sample to consist of  $N$  atoms, each with an initial position  $z_j$ , such that they are randomly distributed along the sample length  $L$  in the  $z$  direction. Since samples in our experiment have a temperature on the order of  $10 \mu\text{K}$ , the spatial extent of their wave functions samples only a very local portion of the SW potential and allows for their motion to be treated more classically. Accordingly, given a far off-resonance SW potential ( $\Delta \gg \Omega_0, \Gamma$ ), aligned along the  $z$  direction, the center of mass of each atom will follow the equation of motion [41]:

$$m\ddot{z}'_j = -\frac{\hbar k \Omega_0^2}{\Delta} \sin(2kz'_j) \quad (7)$$

where  $z'_j$  represents the center of mass position of the  $j$ th atom after the channeling pulse,  $k = 2\pi/\lambda$  is the wave vector of the excitation field,  $m$  is the mass of the atomic species,  $\Delta$  is the detuning of the traveling-wave components of the SW from the excited state, and  $\Omega_0$  is the Rabi frequency of the excitation.

We consider initially stationary atoms and represent the extent of the  $j$ th atom along  $z$  with a probability per unit length  $\Psi_j(z - z'_j) = \psi^* \psi$ , where  $\psi$  is the one-dimensional atomic wave function. Thus, after a channeling pulse of length  $\tau$ , the density of a transverse slice with volume  $V'$  located at a position  $z$  and defined by a longitudinal length  $\delta z$  is described by

$$\rho'(z, \tau) = \frac{1}{V'} \sum_{j=1}^N \int_{z-\delta z/2}^{z+\delta z/2} \Psi_j[z - z'_j(\tau)] dz, \quad (8)$$

where  $\rho'$  is the atomic density of the layer. Here,  $z'_j(\tau)$  represents the center of mass position of the  $j$ th atom after the channeling pulse of duration  $\tau$ , given by the solution to Eq. (7).

To lower the computational cost of evaluating the reflection coefficient, we find that using a delta-function distribution for each atom ( $\Psi_j(z) = \delta_{z,z_j}$ ) is sufficient to model the experimental data. For channeled samples, the spatial width  $\sigma_z \ll \lambda/2$ . Hence, this localized density model is justified for the one-pulse signal. For the two-pulse grating echo AI, the wave packets spread to  $\sigma_z \gg \lambda$ . However, summing over many wave packets with a variety of center positions leads to a reinforcement of the density modulation at the echo time.

We note that the model can be modified to include a more detailed representation of momentum state interference by replacing  $\Psi_j$  in Eq. (8) with a spatially modulated single atom probability distribution. An interesting aspect of such an approach is that it allows the signal envelope in the channeling regime to be predicted despite the absence of an analytical description. We discuss this modification in more detail in Appendix B.

Regardless of the choice of  $\Psi$ , we can use the combination of Eqs. (7) and (8) to calculate the modulated atomic density of the sample. This is consistent with the ‘‘histogram’’ approach followed in Ref. [41] where the position of many atoms was binned after a particular channeling time to generate the population distribution. Nevertheless, for the work presented in the main body of this paper, we only show

simulations using a delta-function distribution for each atom. Here, the density profiles produced by optical channeling, as shown in Fig. 3(e), are computed using Eq. (8) for 1000 atomic trajectories taken at random positions across each SW period  $d$ .

To best match experimental data in both the one-pulse grating AI and the grating echo AI, we define the full ensemble density as

$$\rho(z) = \rho_0(1 - f_R) + f_R\rho'(z) \quad (9)$$

where  $\rho_0$  is atomic density assuming no modulation and  $\rho'$  is the local density modulation calculated using Eq. (7). As shown in Fig. 3(d),  $f_R$  takes on a similar role as in Eq. (1), representing the effective fraction of atoms that are channeled into the lattice. In the case of the grating echo AI, the unmodulated fraction ( $\rho_0$ ) includes the incoherent portions of the atomic wave functions resulting from the spreading of the atomic wave packets in the time between the channeling and readout pulses. We can then use Eqs. (8) and (9) for both AI configurations to partition a channeled ensemble density into thin layers of width  $\delta z$  each with a uniform density. Representative distributions of  $\rho$  are shown in Fig. 3(e) for a variety of channeling times.

From such distributions, it is straightforward to determine the contrast of the gratings given by

$$C = (\max \rho - \min \rho) \quad (10)$$

and the corresponding visibility

$$\mathcal{V} = C/(\max \rho + \min \rho) \quad (11)$$

for arbitrary channeling times. Figure 3(f) shows the visibility predicted by Eq. (11) for a range of channeling times for typical values of  $f_R$  in our experiments inferred by matching data and predictions of simulations. Here we note that  $C$  and  $\mathcal{V}$  exhibit oscillations as a function of the interaction time expressed in units of the harmonic oscillator period for the potential,  $\tau_{\text{HO}} = 2\pi\sqrt{\Delta/\Omega_0^2\omega_q}$ , where  $\omega_q = 2\hbar k^2/m \simeq 2\pi \times 15.5$  kHz is the two-photon recoil frequency [76]. Our experiments typically have  $\tau_{\text{HO}} \approx 6$   $\mu\text{s}$ . We note that for a purely harmonic potential, the visibility reaches a maximum at  $\tau \approx 0.25 \tau_{\text{HO}}$ , while here it reaches a maximum value around  $\tau \approx 0.3 \tau_{\text{HO}}$ , in agreement with the description of an anharmonic potential in Ref. [41].

### C. Application to experimental data

In what follows, we use the experimentally measured atom number  $N$  to calculate the atomic population density in  $K$  sublayers across the sample. Using Eqs. (7)–(9) we describe the spatially varying density resulting from optical channeling pulses of varying lengths. We then compute the reflectivity using the transfer matrix formalism [Eqs. (2)–(6)] for a given readout detuning. In this manner, we are able to characterize the frequency response of the reflectivity for the one-pulse grating AI and grating-echo AI, when the readout beam is tuned near resonance to optimize Bragg scattering.

In our experiments, there are two physical effects which contribute to the alignment of the readout beam relative to the lattice wave vector, which are parametrized by two alignment

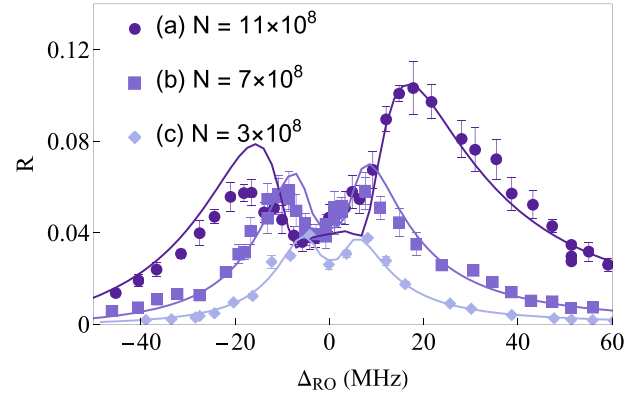


FIG. 4. Reflection coefficient of the one-pulse grating AI as a function of readout detuning for clouds containing different numbers of atoms (shown in legend). Solid lines show simulations using Eq. (6). The excitation pulse has a duration of  $\tau \approx 0.3 \tau_{\text{HO}}$  and the free parameters are determined to be (a)  $f_R = 0.57 \pm 0.03$  and  $\gamma = 0.0 \pm 0.3$  mrad, (b)  $f_R = 0.58 \pm 0.02$  and  $\gamma = 1.5 \pm 0.5$  mrad, and (c)  $f_R = 0.54 \pm 0.01$  and  $\gamma = 1.9 \pm 0.5$  mrad.

angles. We designate  $\Theta$  to represent the angle between the excitation beams relative to  $180^\circ$  that alters the length of the lattice, while we use  $\theta_{\text{RO}}$  to correspond to the angle of incidence of the readout with respect to this lattice wave vector. The alignment of the lattice and readout beams is coarsely maintained at the level of  $\approx 2$  mrad by aligning both the excitation beams and readout beams through the same optical fiber. Since these angles are small, we model their combined effect by defining  $\gamma = \theta_{\text{RO}} - \Theta$ .

We compare experimentally measured reflectivity spectra with predictions of the sequential density model. The model relies on independent measurements of the atom number  $N$  (made with a photodiode) and the sample length  $L$  (made with a CCD camera). In this manner the number of layers and the layer density to be used in the calculations can be determined. We perform a least-squares regression to determine the parameters  $\gamma$  and  $f_R$  that best match the data. We further constrain  $f_R$  to a range between 0 and 1 and  $\gamma$  to lie within our experimental angular uncertainty ( $\approx 2$  mrad).

We use values of  $f_R$  to characterize the visibility of atomic gratings and use Eqs. (9)–(11) to compare with previous grating-echo experiments [77,78]. To quantify the confinement of atoms, we adopt the idealized approach used in Eq. (1) to describe the subset of our experiments that are carried out with an off-resonant readout beam ( $\Delta_{\text{RO}} \approx 50$  MHz). Under these conditions, we demonstrate the  $N^2$  scaling of the peak reflectivity and extract the Debye-Waller factor,  $\beta$ . We also compare the localization of atoms in our experiments with results from previous grating-echo experiments [42].

## IV. RESULTS AND DISCUSSION

Figure 4 shows the reflection coefficient of a one-pulse grating AI as a function of the readout detuning. We find that the scattering spectrum is well modeled by Eq. (6) which includes the effect of channeling. Here, representative calculations are shown as solid lines. As the detuning of the readout beam is decreased, the increase in atom-field coupling leads

to enhanced scattering. Far from resonance, this behavior can also be understood on the basis of Eq. (1), which predicts a Lorentzian dependence for the reflectivity. However, near resonance, the sequential density model predicts a decrease in coherent scattering due to absorptive and multiple scattering effects, a feature prominent in the experimental data, leading to a two-peaked reflectivity spectrum.

For small atom numbers, where absorption is negligible, the model predicts a generally symmetric spectrum with a single peak at zero detuning. For samples with more atoms, the model predicts a two-peaked shape, with a dip near zero detuning due to resonant absorption consistent with Refs. [60,61]. The separation of the two maxima increases in samples with more atoms, as absorption becomes more prevalent at larger readout detunings.

The reflectivity spectrum has a slight inherent asymmetry stemming from the presence of excited states below but not above the  $F = 3 \rightarrow F' = 4'$  transition in  $^{85}\text{Rb}$ , which is also more evident in samples with more atoms. However, as noted in Ref. [60], small changes in the relative angle between the readout wave vector and the lattice beams result in a more prominent asymmetry in the reflection spectrum.

All of these features are represented in the experimental data. However, we note a slight disagreement between the data and simulations near the red-detuned peak of the reflectivity spectrum for samples with  $N > 8 \times 10^8$  atoms. While this discrepancy is not yet well understood, we find excellent agreement in the far-detuned limit, as well as for cases of blue detuned readout beams and for samples with lower numbers of atoms. In our experiments, for samples containing  $\approx 10^9$  atoms, we note an increase in reflectivity by a factor of  $\approx 3$ –4 if the readout detuning is reduced from  $\approx 50$  to  $\approx 18$  MHz.

In calculations of Eq. (6), the interacting fraction  $f_R$  serves as a scale factor representing the occupation number of the lattice and the efficacy of the channeling process. For the one-pulse grating AI, we find that an average value of  $f_R = 0.56 \pm 0.02$  results in the best agreement with data. This value is reflected by the solid line in Fig. 3(f), where we can see that it corresponds to a visibility of  $\mathcal{V} \approx 0.76$ . For our experimental parameters, this maximum visibility for single pulse excitation serves as an upper limit for echo experiments that augment grating contrast using long optical channeling pulses.

Figure 5 shows the reflection coefficient of a grating-echo AI as a function of the readout detuning. Here we note the overall similarity between the echo spectra and their single pulse counterparts shown in Fig. 4, including the dip in reflectivity for small readout detunings in samples with more atoms. In general, we observe a comparable fourfold increase by changing the readout detuning from 50 MHz to the peak value ( $\Delta_{\text{RO}} \approx 20$  MHz).

The agreement between experiment and simulations (solid lines in Fig. 5) shows that Eq. (6) is also successful in modeling the reflection spectra for the grating-echo experiments. Again we leave  $\gamma$  and  $f_R$  as free parameters to best match the experimental data. The values of  $\gamma$ , as reported in the caption, show similar milliradian variation as in one-pulse experiments. These angles explain the slight asymmetry in the spectra, which varies from one data set to another due to slight changes in beam alignment.

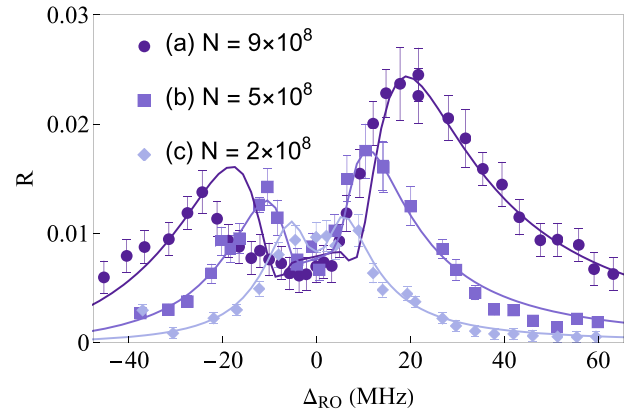


FIG. 5. Reflection coefficient of the grating-echo AI as a function of readout detuning for clouds containing different numbers of atoms (shown in legend). Solid lines show simulations using Eq. (6). Here, the excitation pulses have durations  $\tau \approx 0.3 \tau_{\text{HO}}$  and experiments were performed with a pulse separation  $T = 70.12 \mu\text{s}$ . The free parameters are determined to be (a)  $f_R = 0.26 \pm 0.01$  and  $\gamma = 0.0 \pm 0.5$  mrad, (b)  $f_R = 0.26 \pm 0.02$  and  $\gamma = 0.0 \pm 0.8$  mrad, and (c)  $f_R = 0.27 \pm 0.04$  and  $\gamma = 1.5 \pm 1.5$  mrad.

Although the echo technique faithfully reproduces a density modulation at the echo time, the application of the second pulse is a nonselective process resulting in many interferometric paths, only a subset of which contribute to the signal. This effect, in conjunction with velocity dispersion resulting in the spreading of the atomic wave packets, leads to an overall reduction in the contrast of the density modulation at the echo time in comparison with  $t = 0$ . This change is captured by a reduction in the  $f_R$  parameter in the sequential density model. Accordingly, we find the main difference between Figs. 4 and 5 is the value of  $f_R$ , which is reduced from 0.56 for the one-pulse grating AI to 0.26 for the grating-echo AI.

We show the value of  $f_R = 0.26$  resulting from the grating-echo AI experiments as the dashed line in Fig. 3(f). In Fig. 3(f), we can see that it corresponds to a visibility of  $\mathcal{V} \approx 0.50$ . This visibility can be compared with the maximum theoretical visibility calculated for grating-echo experiments ( $\approx 60\%$ ) in the absence of spontaneous emission and channeling [77,78].

To demonstrate the effect of channeling, we show reflectivity spectra for increasing channeling durations in Figs. 6(a) and 6(b), for the one-pulse grating AI and the grating-echo AI respectively. The agreement between experiment and simulation across a wide range of channeling times, described by Eqs. (7) and (9), serves to illustrate the effectiveness of the model for both AI configurations. For both the one-pulse grating AI and the grating-echo AI, the maximum reflectivity occurs when the channeling time is  $\tau \approx 0.3 \tau_{\text{HO}}$  in agreement with Ref. [41].

Previous echo experiments [36,39,40,53–59], which did not employ channeling, resulted in reflected fractions on the order of  $\approx 0.1\%$  for readout detunings of  $\approx 50$  MHz. We find these values in agreement with our experimental data when the excitation frequency is tuned far off resonance and pulse lengths are restricted to satisfy the Raman-Nath regime

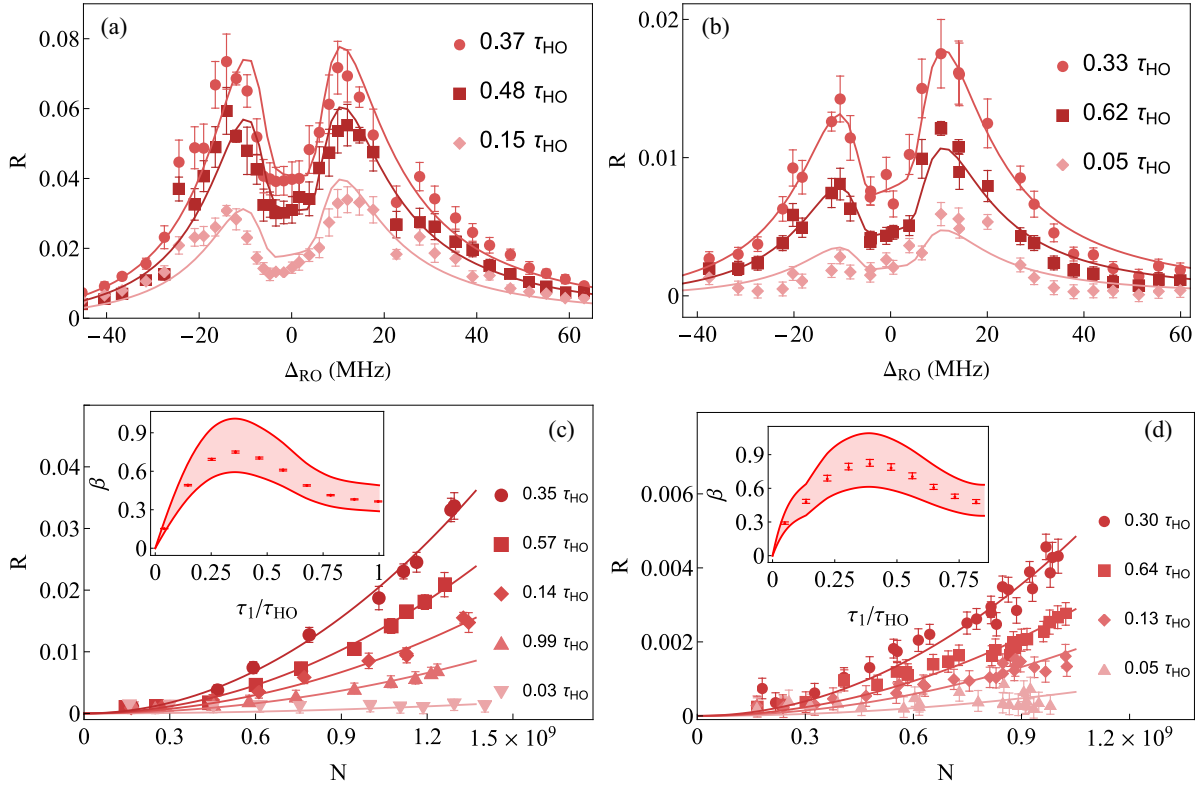


FIG. 6. (a), (b) Reflection coefficient ( $R$ ) as a function of readout detuning resulting for different channeling times in the (a) one-pulse grating AI and (b) the grating-echo AI. Solid lines indicate fits to Eq. (6). For (a),  $N = 7 \times 10^8$ , while  $f_R = 0.57 \pm 0.03$  and  $\gamma = 1.5 \pm 0.5$  mrad best match the results. For (b),  $N = 6 \times 10^8$ , while  $\gamma = 0.1 \pm 0.2$  mrad, and  $f_R = 0.26 \pm 0.03$ . (c), (d)  $R$  as a function of the number of atoms for different channeling times for the one-pulse grating AI (c) and the grating-echo AI (d), respectively. The data in (c) and (d) were collected with a readout detuning of  $\Delta_{RO} = 50$  MHz. The solid lines show quadratic fits to Eq. (1) with  $f_R = 0.57$  for (c) and  $f_R = 0.26$  for (d). The insets in (c) and (d) show the inferred Debye-Waller factor from these fits, with the shaded region representing the experimental uncertainty associated with the number of atoms. Echo experiments in (b) and (d) were performed with a pulse separation  $T = 70.12$   $\mu$ s.

[e.g.,  $\Delta_{RO} \approx 50$  MHz for  $\tau = 0.05 \tau_{HO}$  as in Fig. 6(b)]. Our results indicate that we can improve the reflectivity by nearly a factor of 20 through the combination of optical channeling and near-resonant Bragg scattering [e.g.,  $\Delta_{RO} \approx 15$  MHz for  $\tau = 0.33 \tau_{HO}$  in Fig. 6(b)]. For our best conditions, corresponding to the largest number of atoms loaded into the trap, we report a peak reflectivity of 2.5% (Fig. 5) for the grating-echo AI.

To emphasize the interplay between channeling and the number of atoms in the sample, Figs. 6(c) and 6(d) show the reflectivity as a function of atom number for several channeling times. These data for the one-pulse grating AI (c) and the grating-echo AI (d) were collected using an off-resonance readout ( $\Delta_{RO} \approx 50$  MHz). For each channeling time, we observe the unambiguous quadratic dependence on atom number as predicted by Eq. (1) in the far detuned limit. Using the value of  $f_R$  determined from the spectra shown in Figs. 4 and 5, we can extract the Debye-Waller factor for each channeling time, using Eq. (1). These values are shown in the insets to Figs. 6(c) and 6(d). The peak value of  $\beta \approx 0.78$  coincides with the maximum reflectivity at  $\tau \approx 0.3 \tau_{HO}$ . This value of  $\beta$  corresponds to a confinement of  $0.05 \lambda$  ( $\approx 41$  nm) for both AI configurations. As a point of comparison, Ref. [42] was able to achieve a confinement of 55 nm, by employing channeling which was heavily damped and occurred during the trap loading phase.

## V. CONCLUSIONS

We have presented a thorough exploration of optimized near-resonant Bragg scattering in a grating-echo AI. We have demonstrated that optical channeling pulses, which violate the Raman-Nath criterion, can be used to increase the density modulation of the one-pulse grating AI and the grating-echo AI. We have shown that these high contrast gratings are maximally reflective to near-resonant readout light. We have presented a transfer matrix formalism that is successful at predicting the effects of channeling and Bragg scattering in the sample for both the one-pulse grating AI and the grating-echo AI. Using this model, we have characterized the effectiveness of optical channeling pulses to confine atoms in a lattice using the Debye-Waller factor. The model appears flexible enough to describe changes in the echo envelope as a result of the channeling process when combined with more detailed single atom probability distributions, as discussed in Appendix B. We expect that the model should also be applicable to other coherent scattering experiments where the density of an atomic sample is modulated through laser interaction [79].

For both the one-pulse grating AI and the grating-echo AI, we report a total increase in sample reflectivity of  $\approx 20$  observed by combining the effects of a near-resonant readout beam and optimizing optical channeling. This enhancement is easily observed within a single dataset where the channeling



and detuning parameters have been varied to maximize the signal. It should be possible to realize similar improvements in lattices loaded during the trapping phase of the experiment as in Ref. [42]. We anticipate that these gains will increase the signal-to-noise ratio of the echo AI at large observation times  $T$ , paving the way for more sensitive measurements of  $\hbar/m$  and  $g$ . While we have not yet explored systematic errors introduced by the use of long excitation pulses, we expect that the improved sensitivity of the interferometer will allow these effects to be explored thoroughly and enable a comparison with previously demonstrated AI configurations.

#### ACKNOWLEDGMENTS

This work is supported by Canada Foundation for Innovation, Ontario Innovation Trust, Ontario Centers of Excellence, U.S. Army Research Office (Grant No. W911 NF-12-1-0564), Natural Sciences and Engineering Research Council of Canada, York University, and the Helen Freedhoff Memorial Fund. We also acknowledge helpful discussions with Louis Marmet of York University.

#### APPENDIX A: DERIVATION OF FAR OFF-RESONANT BRAGG REFLECTION

Bragg scattering of a probe beam from a phased array of localized dipoles [50], such as atoms in a lattice, results in the emission of light into a solid angle  $d\Omega$  that can be written as [61,63]

$$\frac{dP}{d\Omega} = \frac{\pi^2}{\lambda_{\text{RO}}^4} \left| \frac{\alpha}{\epsilon_0} \right|^2 (f_R N)^2 \beta^2 I_{\text{in}} \quad (\text{A1})$$

where  $P$  is the scattered power,  $I_{\text{in}}$  is the readout intensity,  $\lambda_{\text{RO}}$  is the readout wavelength,  $N$  is the number of atoms,  $\epsilon_0$  is the permittivity of free space,  $\beta$  is the Debye-Waller factor,  $f_R$  is the fractional occupation number, and

$$\alpha = \frac{3\epsilon_0 \lambda_{\text{RO}}^3}{4\pi^2} \frac{S_{F,F'}}{i + 2\Delta_{\text{RO}}/\Gamma} \quad (\text{A2})$$

is the complex atomic polarizability. Here,  $\Delta_{\text{RO}}$  represents the readout detuning relative to an excited state, where  $\Gamma$  is the radiative rate and  $S_{F,F'}$  is the oscillator strength of the transition.

In the far field, where the scattering atoms can be viewed as a point source, we can estimate the solid angle as  $\Omega \approx 8\lambda_{\text{RO}}^2/\pi D^2$ , where  $D$  is the diameter of the scattered beam.

The resulting scattered power is given by

$$P = 8\pi \frac{(f_R N)^2 \beta^2}{\lambda_{\text{RO}}^2 D^2} \left| \frac{\alpha}{\epsilon_0} \right|^2 I_{\text{in}}. \quad (\text{A3})$$

Assuming that the scattered beam has an intensity

$$I_{\text{scatt}} = \frac{4P}{\pi D^2} \quad (\text{A4})$$

we can write the reflected fraction of the readout field, given by Eq. (1), as

$$R = \frac{I_{\text{scatt}}}{I_{\text{in}}} = \frac{18}{\pi^4} \left( \frac{\lambda_{\text{RO}}}{D} \right)^4 \frac{S_{F,F'}^2}{1 + (2\Delta_{\text{RO}}/\Gamma)^2} (f_R N)^2 \beta^2. \quad (\text{A5})$$

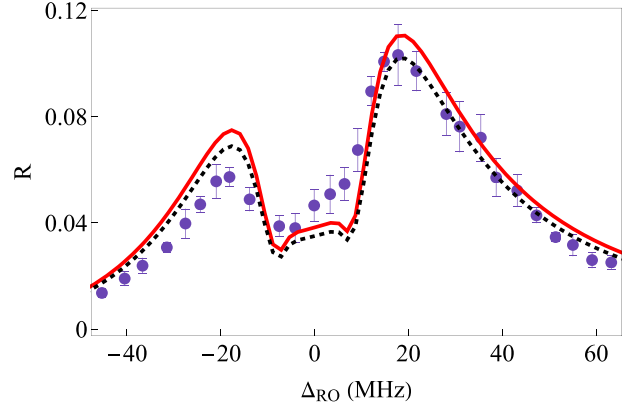


FIG. 7. One-pulse grating AI reflection coefficient in comparison with simulations of Eq. (6). Simulations use  $N = 11 \times 10^8$ ,  $f_R = 0.56$ , and  $\gamma = 0.0$  mrad. The solid line indicates simulations with  $\Psi = \delta_{z,z_j}$  while the dashed line represents simulations using a Gaussian wave packet with a width of  $\hbar/\sigma_p$ .

#### APPENDIX B: REFLECTIVITY FOR ALTERNATE SINGLE ATOM PROBABILITY DISTRIBUTION

As mentioned in Sec. III, the transfer matrix formalism and sequential density model can be modified to incorporate additional physical effects present in the interferometer. In the main body of the paper we employ a delta function to represent the single-atom probability distribution. Here, we show two examples of how the sequential density model can be applied to other single-atom probability distributions. The first is a Gaussian distribution and the second is a distribution with spatial modulation that arises from interaction with short laser pulses in the Raman-Nath limit.

As described in the body of the paper, the atomic probability distribution  $\Psi_j = \psi^* \psi$  can be approximated by a delta function even for relatively hot atomic samples. This simplification can be avoided by using a Gaussian wave packet with a spatial width of  $\hbar/\sigma_p$ . Here,  $\sigma_p = \sqrt{2mk_B T}$  is the momentum-space width of an atomic probability distribution with temperature  $T$ , and  $k_B$  is Boltzmann's constant. Examples of the spectra including this Gaussian distribution and the delta function approximation are shown with accompanying experimental data in Fig. 7, where we see no significant difference arising from the relatively narrow spread of wave packets for 10- $\mu$ K samples.

In addition, the transfer matrix approach can also be used to describe the time dependent envelope of the scattered field signal in the grating-echo AI in the channeling regime, where an analytical description is not available.

In previous work [36,41,53,59], the signal shape in the Raman-Nath regime has been estimated by calculating the atomic density ( $\Psi = \psi^* \psi$ ), integrating over the velocity distribution, and evaluating the  $\lambda/2$  Fourier component. The solid lines in the lower panels of Fig. 1 show the signal shapes resulting from this type of calculation for pulses that satisfy the Raman-Nath criterion. However, by altering the atomic probability distribution  $\Psi$  in Eq. (8) to include momentum state interference, and then inserting this new distribution into the transfer matrix formalism, we can predict the signal shape

both in the Raman-Nath regime and for the channeling regime in which excitation pulses violate the Raman-Nath criterion.

As an example, we can use the modulated position-space wave function following the application of two SW pulses separated by a time  $T$ , that was derived in the absence of spontaneous emission and atomic motion [71] as

$$\begin{aligned} \psi_2(z, t) = & \left( \frac{\sigma_p}{\sqrt{\pi} \hbar F(t)} \right)^{1/2} e^{-\frac{(z\hbar)^2}{2\sigma_p^2 F(t)}} \\ & \times \sum_{n, n'} A_n B_{n'} e^{i(n\phi_1 + n'\phi_2)} e^{\frac{-i}{F(T)} p_n^2 T / 2m\hbar} \\ & \times e^{\frac{-i}{F(T)} P_{n, n'}^2 (t-T) / 2m\hbar} e^{\frac{i}{F(T)} P_{n, n'} z / \hbar}. \end{aligned} \quad (\text{B1})$$

Here  $\phi_1$  is the phase of the first SW excitation and  $F(t) = 1 + i\omega_D t$  describes the spreading of the wave function due to the Doppler angular frequency width  $\omega_D = 2k_B T / \hbar$ . The coefficients  $A_n = (-i)^n J_n(u_1)$  correspond to  $n$ th order Bessel functions ( $J_n$ ) arising from a Jacobi-Anger expansion for a first pulse area  $u_1 = \Omega_0^2 \tau_1 / 2\Delta$ .  $B_{n'} = (-i)^{n'} J_{n'}(u_2)$ , where  $u_2 = \Omega_0^2 \tau_2 / 2\Delta$  is the second pulse area,  $\phi_2$  is the phase of the second pulse,  $p_n = p_0 + n\hbar q$  is the momentum state excited by the first SW pulse, and  $P_{n, n'} = p_0 + (n + n'F(T))\hbar q$  is the total momentum excited by the two pulses. In this case,  $q = 2k$  is the lattice wave vector and  $p_0$  is the mean momentum of the sample.

Figure 8 shows the results of using the wave functions from Eq. (B1) in the sequential density simulations described in the main body of this paper. Here we take  $\Psi = \psi_2^* \psi_2$ , and insert it into a calculation of the atomic density distribution [Eq. (8)] in order to calculate the reflectivity in the vicinity of  $t = 2T$ . The resulting calculations based on Eq. (6) are overlaid with experimental data showing the echo envelope. Here the envelope data were obtained by varying the onset of the readout pulse relative to the echo time ( $t = 2T$ ).

These simulations were performed by using Monte Carlo methods and by limiting the population of the atomic lattice to  $N = 1000$  atoms, as the computational costs of using a more realistic  $N$  were prohibitive. Accordingly, the absolute value of the reflectivity was scaled by an arbitrary constant to match the data.

Despite this rescaling, we note the good agreement between simulation and data, demonstrating the transition of the echo envelope from a two-lobed feature in the Raman-Nath regime ( $\tau \approx 0.17 \tau_{\text{HO}}$ ) to a single-lobed feature in the channeling regime ( $\tau \approx 1.07 \tau_{\text{HO}}$ ). This change in signal shape has been remarked upon in Ref. [42] but does not appear to have been studied further.

We can explain this result using the billiard ball model presented in Fig. 1, where the signal maxima will occur

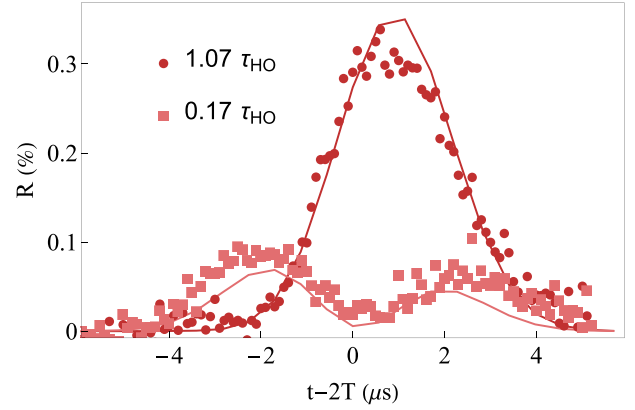


FIG. 8. Signal envelopes of the grating-echo AI as a result of different channeling times as indicated by the legend. Points indicate experimental data while solid lines show simulations of the sample reflectivity predicted by Eq. (6) with a probability distribution of a single atom defined by (B1) which represents the matter-wave interference created by the excitation pulses.

when diffracting wave packets partially overlap within their de Broglie wavelengths [78], both immediately after the first pulse or near the echo time. In the Raman-Nath limit, one can consider the excitation pulses to be imposing a phase grating on the atomic sample which must then evolve into a population density grating before it is probed using coherent scattering of the RO pulse. It is for this reason that the one-pulse density grating takes some time to evolve after the application of the first SW pulse [41] in the Raman-Nath regime, as shown in Fig. 1. In the echo AI, the second excitation pulse reestablishes the density modulation that was present at  $t = 0$  at the echo time  $t = 2T$ . Accordingly, in the Raman-Nath regime, the sample will be returned to an initially unmodulated state at  $t = 2T$ , resulting in a zero in the reflectivity. However, if the sample is optically channeled, then the second pulse will recreate the channeled density grating at the echo time rather than simply in its vicinity, resulting in a signal maxima at  $t = 2T$ , as shown in Fig. 8.

We expect that improvements in the Monte Carlo simulation should eliminate the need for rescaling. Likewise, alterations to the modulated atomic wave function to include the effects of spontaneous emission [53] and atomic motion during the excitation pulses should lead to even better agreement with experimental results. The sequential density model is sufficiently flexible to accommodate such changes, and this aspect can lead to an interesting avenue for future exploration.

- [1] M. Kasevich and S. Chu, Atomic interferometry using stimulated Raman transitions, *Phys. Rev. Lett.* **67**, 181 (1991).  
 [2] A. Peters, K. Y. Chung, and S. Chu, Measurement of gravitational acceleration by dropping atoms, *Nature (London)* **400**, 849 (1999).

- [3] K. Gibble and S. Chu, Laser-cooled Cs frequency standard and a measurement of the frequency shift due to ultracold collisions, *Phys. Rev. Lett.* **70**, 1771 (1993).  
 [4] D. S. Weiss, B. C. Young, and S. Chu, Precision measurement of  $\hbar/m$  Cs based on photon recoil using laser-cooled atoms and atomic interferometry, *Appl. Phys. B* **59**, 217 (1994).

- [5] M. J. Snadden, J. M. McGuirk, P. Bouyer, K. G. Haritos, and M. A. Kasevich, Measurement of the Earth's gravity gradient with an atom interferometer-based gravity gradiometer, *Phys. Rev. Lett.* **81**, 971 (1998).
- [6] J. M. McGuirk, G. T. Foster, J. B. Fixler, M. J. Snadden, and M. A. Kasevich, Sensitive absolute-gravity gradiometry using atom interferometry, *Phys. Rev. A* **65**, 033608 (2002).
- [7] Z.-K. Hu, B.-L. Sun, X.-C. Duan, M.-K. Zhou, L.-L. Chen, S. Zhan, Q.-Z. Zhang, and J. Luo, Demonstration of an ultrahigh-sensitivity atom-interferometry absolute gravimeter, *Phys. Rev. A* **88**, 043610 (2013).
- [8] V. Xu, M. Jaffe, C. D. Panda, S. L. Kristensen, L. W. Clark, and H. Müller, Probing gravity by holding atoms for 20 seconds, *Science* **366**, 745 (2019).
- [9] G. M. Tino, L. Cacciapuoti, S. Capozziello, G. Lambiase, and F. Sorrentino, Precision gravity tests and the einstein equivalence principle, *Prog. Part. Nucl. Phys.* **112**, 103772 (2020).
- [10] L. Morel, Z. Yao, P. Cladé, and S. Guellati-Khélifa, Determination of the fine-structure constant with an accuracy of 81 parts per trillion, *Nature (London)* **588**, 61 (2020).
- [11] R. H. Parker, C. Yu, W. Zhong, B. Estey, and H. Müller, Measurement of the fine-structure constant as a test of the standard model, *Science* **360**, 191 (2018).
- [12] P. Cladé, E. de Mirandes, M. Cadoret, S. Guellati-Khélifa, C. Schwob, F. Nez, L. Julien, and F. Biraben, Determination of the fine structure constant based on Bloch oscillations of ultracold atoms in a vertical optical lattice, *Phys. Rev. Lett.* **96**, 033001 (2006).
- [13] P. Cladé, E. de Mirandes, M. Cadoret, S. Guellati-Khélifa, C. Schwob, F. Nez, L. Julien, and F. Biraben, Precise measurement of  $h/m_{Rb}$  using Bloch oscillations in a vertical optical lattice: Determination of the fine-structure constant, *Phys. Rev. A* **74**, 052109 (2006).
- [14] M. Cadoret, E. De Mirandes, P. Cladé, S. Guellati-Khélifa, C. Schwob, F. Nez, L. Julien, and F. Biraben, Precise determination of  $h/m_{Rb}$  using Bloch oscillations and atomic interferometry: A mean to deduce the fine structure constant, *Eur. Phys. J.: Spec. Top.* **163**, 101 (2008).
- [15] C. Yu, W. Zhong, B. Estey, J. Kwan, R. H. Parker, and H. Müller, Atom-interferometry measurement of the fine structure constant, *Ann. Phys. (Leipzig)* **531**, 1800346 (2019).
- [16] G. Lamporesi, A. Bertoldi, L. Cacciapuoti, M. Prevedelli, and G. M. Tino, Determination of the Newtonian gravitational constant using atom interferometry, *Phys. Rev. Lett.* **100**, 050801 (2008).
- [17] A. Bertoldi, G. Lamporesi, L. Cacciapuoti, M. de Angelis, M. Fattori, T. Petelski, A. Peters, M. Prevedelli, J. Stuhler, and G. M. Tino, Atom interferometry gravity-gradiometer for the determination of the Newtonian gravitational constant  $G$ , *Eur. Phys. J. D* **40**, 271 (2006).
- [18] J. B. Fixler, G. T. Foster, J. M. McGuirk, and M. A. Kasevich, Atom interferometer measurement of the Newtonian constant of gravity, *Science* **315**, 74 (2007).
- [19] B. Battelier, B. Barrett, L. Fouché, L. Chichet, L. Antoni-Micollier, H. Porte, F. Napolitano, J. Lautier, A. Landragin, and P. Bouyer, Development of compact cold-atom sensors for inertial navigation, in *Quantum Optics*, edited by J. Stuhler and A. J. Fields, Proceedings of SPIE Vol. 9900 (SPIE, Bellingham, WA, 2016), pp. 21–37.
- [20] Y. Bidel, N. Zahzam, C. Blanchard, A. Bonnin, M. Cadoret, A. Bresson, D. Rouxel, and M. Lequentrec-Lalancette, Absolute marine gravimetry with matter-wave interferometry, *Nat. Commun.* **9**, 627 (2018).
- [21] Y. Bidel, N. Zahzam, A. Bresson, C. Blanchard, M. Cadoret, A. V. Olesen, and R. Forsberg, Absolute airborne gravimetry with a cold atom sensor, *J. Geod.* **94**, 20 (2020).
- [22] B. Stray, A. Lamb, A. Kaushik, J. Vovrosh, A. Rodgers, J. Winch, F. Hayati, D. Boddice, A. Stabrawa, A. Niggebaum *et al.*, Quantum sensing for gravity cartography, *Nature (London)* **602**, 590 (2022).
- [23] X. Wu, Z. Pagel, B. S. Malek, T. H. Nguyen, F. Zi, D. S. Scheirer, and H. Müller, Gravity surveys using a mobile atom interferometer, *Sci. Adv.* **5**, eaax0800 (2019).
- [24] A. López-Vázquez, M. Maldonado, E. Gomez, N. Corzo, E. de Carlos-López, J. F. Villafañe, K. Jiménez-García, J. Jimenez-Mier, J. López-González, C. López-Monjaraz *et al.*, Compact laser modulation system for a transportable atomic gravimeter, *Opt. Express* **31**, 3504 (2023).
- [25] A. D. Cronin, J. Schmiedmayer, and D. E. Pritchard, Optics and interferometry with atoms and molecules, *Rev. Mod. Phys.* **81**, 1051 (2009).
- [26] G. M. Tino *et al.*, Testing gravity with atom interferometry, *Atom Interferometry* **188**, 457 (2014).
- [27] P. Cheinet, B. Canuel, F. P. Dos Santos, A. Gauguet, F. Yver-Leduc, and A. Landragin, Measurement of the sensitivity function in a time-domain atomic interferometer, *IEEE Trans. Instrum. Meas.* **57**, 1141 (2008).
- [28] P. J. Martin, P. L. Gould, B. G. Oldaker, A. H. Miklich, and D. E. Pritchard, Diffraction of atoms moving through a standing light wave, *Phys. Rev. A* **36**, 2495 (1987).
- [29] P. J. Martin, P. L. Gould, B. G. Oldaker, A. H. Miklich, and D. E. Pritchard, Diffraction of atoms from a standing light wave, *Physica B+C* **151**, 255 (1988).
- [30] G. D'Amico, F. Borselli, L. Cacciapuoti, M. Prevedelli, G. Rosi, F. Sorrentino, and G. M. Tino, Bragg interferometer for gravity gradient measurements, *Phys. Rev. A* **93**, 063628 (2016).
- [31] E. Giese, A. Roura, G. Tackmann, E. M. Rasel, and W. P. Schleich, Double Bragg diffraction: A tool for atom optics, *Phys. Rev. A* **88**, 053608 (2013).
- [32] D. M. Giltner, R. W. McGowan, and S. A. Lee, Atom interferometer based on Bragg scattering from standing light waves, *Phys. Rev. Lett.* **75**, 2638 (1995).
- [33] T. Mazzoni, X. Zhang, R. Del Aguila, L. Salvi, N. Poli, and G. M. Tino, Large-momentum-transfer Bragg interferometer with strontium atoms, *Phys. Rev. A* **92**, 053619 (2015).
- [34] S. S. Szigeti, J. E. Debs, J. J. Hope, N. P. Robins, and J. D. Close, Why momentum width matters for atom interferometry with Bragg pulses, *New J. Phys.* **14**, 023009 (2012).
- [35] P. Altin, M. Johnsson, V. Negnevitsky, G. Dennis, R. P. Anderson, J. Debs, S. Szigeti, K. Hardman, S. Bennetts, G. McDonald *et al.*, Precision atomic gravimeter based on Bragg diffraction, *New J. Phys.* **15**, 023009 (2013).
- [36] S. B. Cahn, A. Kumarakrishnan, U. Shim, T. Sleator, P. R. Berman, and B. Dubetsky, Time-domain de Broglie wave interferometry, *Phys. Rev. Lett.* **79**, 784 (1997).
- [37] B. Barrett, I. Chan, C. Mok, A. Carew, I. Yavin, A. Kumarakrishnan, S. B. Cahn, and T. Sleator, Time-domain interferometry with laser-cooled atoms, in *Advances in Atomic,*

- Molecular, and Optical Physics* (Elsevier, Amsterdam, 2011), Vol. 60, pp. 119–199.
- [38] B. Barrett, A. Carew, H. C. Beica, A. Vorozcovs, A. Pouliot, and A. Kumarakrishnan, Prospects for precise measurements with echo atom interferometry, *Atoms* **4**, 19 (2016).
- [39] B. Barrett, A. Carew, S. Beattie, and A. Kumarakrishnan, Measuring the atomic recoil frequency using a modified grating-echo atom interferometer, *Phys. Rev. A* **87**, 033626 (2013).
- [40] C. Mok, B. Barrett, A. Carew, R. Berthiaume, S. Beattie, and A. Kumarakrishnan, Demonstration of improved sensitivity of echo interferometers to gravitational acceleration, *Phys. Rev. A* **88**, 023614 (2013).
- [41] G. Carlse, J. Randhawa, E. Ramos, T. Vacheresse, A. Pouliot, A. C. Carew, and A. Kumarakrishnan, Role of optical channeling in contrast enhancement of echo interferometers, *Phys. Rev. A* **109**, 043307 (2024).
- [42] M. F. Andersen and T. Sleator, Lattice interferometer for laser-cooled atoms, *Phys. Rev. Lett.* **103**, 070402 (2009).
- [43] J. F. Clauser and S. Li, Talbot-Vonlau atom interferometry with cold slow potassium, *Phys. Rev. A* **49**, R2213 (1994).
- [44] M. S. Chapman, C. R. Ekstrom, T. D. Hammond, J. Schmiedmayer, B. E. Tannian, S. Wehinger, and D. E. Pritchard, Near-field imaging of atom diffraction gratings: The atomic Talbot effect, *Phys. Rev. A* **51**, R14 (1995).
- [45] P. R. Berman and V. S. Malinovsky, *Principles of Laser Spectroscopy and Quantum Optics* (Princeton University, Princeton, NJ, 2011).
- [46] P. R. Berman, *Atom Interferometry* (Academic Press, New York, 1997).
- [47] P. Kapitza and P. Dirac, The reflection of electrons from standing light waves, in *Mathematical Proceedings of the Cambridge Philosophical Society* (Cambridge University, New York, 1933), Vol. 29, pp. 297–300.
- [48] P. L. Gould, G. A. Ruff, and D. E. Pritchard, Diffraction of atoms by light: The near-resonant Kapitza-Dirac effect, *Phys. Rev. Lett.* **56**, 827 (1986).
- [49] R. Beach, S. R. Hartmann, and R. Friedberg, Billiard-ball echo model, *Phys. Rev. A* **25**, 2658 (1982).
- [50] I. Abella, N. Kurnit, and S. Hartmann, Photon echoes, *Phys. Rev.* **141**, 391 (1966).
- [51] S. Gupta, K. Dieckmann, Z. Hadzibabic, and D. E. Pritchard, Contrast interferometry using bose-einstein condensates to measure  $h/m$  and  $\alpha$ , *Phys. Rev. Lett.* **89**, 140401 (2002).
- [52] A. O. Jamison, B. Plotkin-Swing, and S. Gupta, Advances in precision contrast interferometry with Yb Bose-Einstein condensates, *Phys. Rev. A* **90**, 063606 (2014).
- [53] S. Beattie, B. Barrett, M. Weel, I. Chan, C. Mok, S. B. Cahn, and A. Kumarakrishnan, Influence of spontaneous emission on a single-state atom interferometer, *Phys. Rev. A* **77**, 013610 (2008).
- [54] S. Beattie, B. Barrett, I. Chan, C. Mok, I. Yavin, and A. Kumarakrishnan, Technique for measuring atomic recoil frequency using coherence functions, *Phys. Rev. A* **79**, 021605(R) (2009).
- [55] S. Beattie, B. Barrett, I. Chan, C. Mok, I. Yavin, and A. Kumarakrishnan, Atom-interferometric studies of light scattering, *Phys. Rev. A* **80**, 013618 (2009).
- [56] M. Weel and A. Kumarakrishnan, Observation of ground-state Ramsey fringes, *Phys. Rev. A* **67**, 061602(R) (2003).
- [57] M. Weel, I. Chan, S. Beattie, A. Kumarakrishnan, D. Gosset, and I. Yavin, Effect of a magnetic field gradient and gravitational acceleration on a time-domain grating-echo interferometer, *Phys. Rev. A* **73**, 063624 (2006).
- [58] B. Barrett, I. Chan, and A. Kumarakrishnan, Atom-interferometric techniques for measuring uniform magnetic field gradients and gravitational acceleration, *Phys. Rev. A* **84**, 063623 (2011).
- [59] B. Barrett, Techniques for measuring the atomic recoil frequency using a grating-echo atom interferometer, Ph.D. thesis, York University, 2012.
- [60] G. Birkl, M. Gatzke, I. H. Deutsch, S. L. Rolston, and W. D. Phillips, Bragg scattering from atoms in optical lattices, *Phys. Rev. Lett.* **75**, 2823 (1995).
- [61] S. Slama, C. von Cube, M. Kohler, C. Zimmermann, and P. W. Courteille, Multiple reflections and diffuse scattering in Bragg scattering at optical lattices, *Phys. Rev. A* **73**, 023424 (2006).
- [62] G. Carlse, J. Randhawa, A. Pouliot, T. Vacheresse, E. Ramos, A. Carew, and A. Kumarakrishnan, Improving the sensitivity grating-echo atom interferometers for measurements of gravity, in *Quantum Sensing, Imaging, and Precision Metrology II*, edited by J. Scheuer and S. M. Shahriar, Proceedings of SPIE Vol. 12912 (SPIE, Bellingham, WA, 2024), pp. 155–159.
- [63] M. Weidemüller, A. Hemmerich, A. Görlitz, T. Esslinger, and T. W. Hänsch, Bragg diffraction in an atomic lattice bound by light, *Phys. Rev. Lett.* **75**, 4583 (1995).
- [64] C. Monroe, W. Swann, H. Robinson, and C. Wieman, Very cold trapped atoms in a vapor cell, *Phys. Rev. Lett.* **65**, 1571 (1990).
- [65] H. C. Beica, A. Pouliot, A. Carew, A. Vorozcovs, N. Afkhami-Jeddi, G. Carlse, P. Dowling, B. Barron, and A. Kumarakrishnan, Characterization and applications of auto-locked vacuum-sealed diode lasers for precision metrology, *Rev. Sci. Instrum.* **90**, 085113 (2019).
- [66] A. Pouliot, H. C. Beica, A. Carew, A. Vorozcovs, G. Carlse, and A. Kumarakrishnan, Auto-locking waveguide amplifier system for lidar and magnetometric applications, in *High-Power Diode Laser Technology XVI*, edited by M. S. Zediker, Proceedings of SPIE Vol. 10514 (SPIE, Bellingham, WA, 2018), pp. 152–159.
- [67] A. Vorozcovs, M. Weel, S. Beattie, S. Cauchi, and A. Kumarakrishnan, Measurements of temperature scaling laws in an optically dense magneto-optical trap, *J. Opt. Soc. Am. B* **22**, 943 (2005).
- [68] G. Carlse, A. Pouliot, T. Vacheresse, A. Carew, H. Beica, S. Winter, and A. Kumarakrishnan, Technique for magnetic moment reconstruction of laser-cooled atoms using direct imaging and prospects for measuring magnetic sublevel distributions, *JOSA B* **37**, 1419 (2020).
- [69] E. A. Donley, T. P. Heavner, F. Levi, M. Tataw, and S. R. Jefferts, Double-pass acousto-optic modulator system, *Rev. Sci. Instrum.* **76**, 063112 (2005).
- [70] S. Cauchi, A. Vorozcovs, M. Weel, S. Beattie, O. Gagnon, and A. Kumarakrishnan, Absorption spectroscopy of trapped rubidium atoms, *Can. J. Phys.* **82**, 905 (2004).
- [71] A. C. Carew, Apparatus for inertial sensing with cold atoms, Ph.D. thesis, York University, 2018.
- [72] A. Schilke, C. Zimmermann, P. W. Courteille, and W. Guerin, Photonic band gaps in one-dimensionally ordered cold atomic vapors, *Phys. Rev. Lett.* **106**, 223903 (2011).



- [73] C. Kittel and P. McEuen, *Introduction to Solid State Physics* (Wiley, New York, 2018).
- [74] I. H. Deutsch, R. J. C. Spreeuw, S. L. Rolston, and W. D. Phillips, Photonic band gaps in optical lattices, *Phys. Rev. A* **52**, 1394 (1995).
- [75] M. Artoni, G. La Rocca, and F. Bassani, Resonantly absorbing one-dimensional photonic crystals, *Phys. Rev. E* **72**, 046604 (2005).
- [76] In Ref. [41] this definition of the harmonic oscillator period has a typographical error, omitting the leading factor of 2.
- [77] A. Tonyushkin, Comment on “Periodic structures generated in a cloud of cold atoms,” *Phys. Rev. A* **75**, 037602 (2007).
- [78] D. V. Strekalov, A. Turlapov, A. Kumarakrishnan, and T. Sleator, Periodic structures generated in a cloud of cold atoms, *Phys. Rev. A* **66**, 023601 (2002).
- [79] A. Pouliot, G. Carlse, H. C. Beica, T. Vacheresse, A. Kumarakrishnan, U. Shim, S. B. Cahn, A. Turlapov, and T. Sleator, Accurate determination of an alkali-vapor-inert-gas diffusion coefficient using coherent transient emission from a density grating, *Phys. Rev. A* **103**, 023112 (2021).